Spring 2022

Plasticity Characterization by Deriving Non-Linear Displacements for In-Plane Biaxial Cruciform Testing

Jordan Michaela Hoffman
University of New Hampshire, Durham

PLASTICITY CHARACTERIZATION BY DERIVING NON-LINEAR DISPLACEMENT PATHS FOR IN-PLANE BIAXIAL CRUCIFORM TESTS

BY

JORDAN M. HOFFMAN

Baccalaureate of Science, University of New Hampshire, 2021

THESIS

Submitted to the University of New Hampshire

in Patrial Fulfillment of

the Requirements of the Degree of

Master of Science

in

Mechanical Engineering

May 2022

This thesis has been examined and approved in partial fulfillment of the requirements for the degree of Master of Science in Mechanical Engineering by:

Thesis Director, Jinjin Ha,

Assistant Professor of Mechanical Engineering

Brad L. Kinsey,

Professor of Mechanical Engineering

Dilip K. Banerjee,

Research Engineer

National Institute of Standards and Technology

Mark A. Iadicola

Research Engineer

National Institute of Standards and Technology

On May 6th, 2022

Other approval signatures are on file with the University of New Hampshire Graduate School.

ACKNOWLEDGEMENTS

I would like to thank my advisors Dr. Jinjin Ha and Dr. Brad Kinsey for their guidance and support throughout this research experience.

I also want to thank Dr. Dilip Banerjee and Dr. Mark Iadicola for the opportunity to work with them as an Undergraduate Research Fellow and for their sustained guidance in the continuation of this research.

I am sincerely grateful to the National Institute of Standards and Technology for their support through the Summer Undergraduate Research Fellowship Program.

I acknowledge and thank the National Science Foundation for their support via the NH BioMade EPSCoR award (#1757371).

Thank you to Elizabeth Mamros, Sarah Mayer, and Riley Desmarais for their assistance and contributions to this works.

Lastly, I would like to thank all my friends, family, and mentors for their endless support and encouragement.

TABLE OF CONTENTS

ACKNOWLEDGEMENTS ..... **III**

TABLE OF CONTENTS ..... **IV**

LIST OF FIGURES ..... **VI**

ABSTRACT ..... **VIII**

CHAPTER 1 ..... **1**

ABSTRACT 2

1. INTRODUCTION 2

2. INTERPOLATION METHOD 3

3. FINITE ELEMENT MODEL 3

4. DOUBLE INTERPOLATION 4

5. CONCLUSION 5

ACKNOWLEDGEMENTS 5

DISCLAIMER 5

REFERENCES 6

CHAPTER 2 ..... **1**

1. INTRODUCTION 2

2. REVIEW OF INTERPOLATION METHOD 6

3. LINEARIZATION OF STRESS PATH USING INVERSE METHOD 11

3.1 FINITE ELEMENT MODEL 11

3.2 RESULTS 15

4. CONCLUSION 27

APPENDICES 28

REFERENCES 29

LIST OF FIGURES

Figure 1.1: Schematic description of interpolation method 3

Figure 1.2 FE model of cruciform geometry 4

Figure 1.3 ASTM A1008 Steel stress-strain curve 4

Figure 1.4 Results of initial interpolation of plane strain path 4

Figure 1.5 Results of double interpolation compared to single interpolation 5

Figure 1.6 Displacement path comparison of double interpolation, single interpolation, and linear 5

Figure 2.1. Varied martensite transformation kinetics for various stress states..... 3

Figure 2.2 Schematic of interpolation method 7

Figure 2.3 Schematic of iterative progression of interpolation method 10

Figure 2.4 Cruciform Geometry 12

Figure 2.5 1/8th cruciform model..... 14

Figure 2.6 Five target linear stress curves 16

Figure 2.7 A) Nine stress reference curves B) Linear input displacements for reference curves..... 18

Figure 2.8 Progression of pure shear (1:-1) stress interpolation. A) Stress, B) Displacement, and C) Stress triaxiality..... 20

Figure 2.9 Resulting stress produced by interpolated displacement paths..... 23

Figure 2.10 Interpolated displacement paths corresponding to five stress states 24

Figure 2.11 Stress Triaxiality extracted from simulations of interpolated displacement. 26

LIST OF TABLES

Table 2.1 Experimentally determined Hockett-Sherby model parameters..... 13

Table 2.2 Progression of 1:-1 interpolation termination criteria over successive iterations 21

Table 2.3 Termination Criteria values for final interpolation of each stress state. 26

ABSTRACT

In-plane biaxial testing using a cruciform type specimen is a useful experimental method to characterize the elasto-plastic material behavior under non-uniaxial conditions. Different stress states can be imposed to the specimen simply by varying loading ratios along two orthogonal axes. Experiments can be performed using one experimental setup and one specimen geometry. Among different control options for loading, the displacement control in each arm is a stable and consistent option to keep the static deformation rate. However, a non-linear relationship exists between the control parameter e.g., displacement, and derived quantities, e.g., stress and strain. Therefore, it is a challenge to achieve desired deformation paths in the main deformation area of the specimen. In this document, an interpolation method to systematically determine non-linear displacement paths is implemented using the finite element simulation method to produce linear stress and strain paths in the center of a cruciform specimen geometry. Interpolation is first applied to an AISI 1008 steel specimen, in which a previously interpolated linear strain path is improved with another iteration of interpolation. Interpolation is then expanded to produce displacement paths resulting in linear stress paths, having a constant stress triaxiality, for five different stress states of a SS304L cruciform specimen. The versatility of the interpolation method is displayed through the successful implementation for both strain and stress linearization as well as with two different materials and two specimen geometries.

CHAPTER 1

DOUBLE INTERPOLATION TO ACHIEVE LINEAR STRAIN PATH FOR AISI 1008 STEEL CRUCIFORM SPECIMEN

(ACCEPTED TO THE 2022 MANUFACTURING SCIENCE AND ENGINEERING CONFERENCE)

Proceedings of the ASME 2022 17th International Manufacturing Science and Engineering Conference
MSEC2022
June 27-July 1, 2022, West Lafayette, Indiana, USA

MSEC2022-85595

DOUBLE INTERPOLATION TO ACHIEVE LINEAR STRAIN PATH FOR AISI 1008 STEEL CRUCIFORM SPECIMEN

Jordan Hoffman
University of New Hampshire
Durham, NH

Jinjin Ha
University of New Hampshire
Durham, NH

Brad Kinsey
University of New Hampshire
Durham, NH

Dilip Banerjee
National Institute of Standards and Technology
Gaithersburg, MD

Mark A. Iadicola
National Institute of Standards and Technology
Gaithersburg, MD

ABSTRACT

The automotive industry relies heavily on sheet metal forming processes for many components. Material data solely from uniaxial testing is insufficient to fully define the material behavior of the complex plastic deformation during numerical simulations of the forming processes. In-plane biaxial testing using a cruciform type specimen is a more comprehensive representation than the traditional uniaxial testing alone. Wide ranging biaxial stress states can be imposed by applying different loading conditions on each cruciform axis. However, this can create a challenge to achieve desired deformation paths due to the non-linear relationship between the control parameter, e.g., displacement, and the output of interest, e.g., strain path. In this paper, an interpolation method to develop the displacement control that produces a linear strain path with a desired strain ratio is revisited and expanded upon from the authors' previous work [1,2]. In the first iteration, linear biaxial displacements were applied to the specimen and the corresponding strain paths were obtained from the numerical simulations. The non-linear strain paths, due to geometry effects of the specimen, were used to reverse engineer a new displacement path that results in a linear strain path. Interpolation is revisited to show increased success with a second iteration. Analysis of the simulation results shows that linear strain paths of a given model can be determined and improved by successive iterations of interpolating the strain data from adjacent deformation paths.

1. INTRODUCTION

Sheet metal forming is known to produce high quantities of parts with consistent quality, notably for the automotive industry. The implementation of the forming process, however, can be challenging due to the lack of agreement between predictive simulations and actual process parts. This discrepancy is partially caused by using only uniaxial test data in the simulations to characterize the material behavior, which does not represent the multiaxial nature of the actual process. There is a need to produce material data under various stress states to capture the complexities introduced by multiaxial deformation.

Biaxial tension testing using a cruciform specimen to produce multiaxial data could aid in the development of new or improved material models for forming simulations. In this test, specimens are loaded in two orthogonal directions in the plane of the sheet. Material response (i.e., force-displacement and strain data) can be collected via measurement systems, such as a load cell, displacement sensor, and digital image correlation (DIC) respectively [3]. Most in-plane biaxial tension machines operate using a prescribed signal-based control system, such as force or displacement. However, the applied deformation path to the control system does not guarantee the specific strain deformation in the gauge area that the user desires. This requires a method to systematically adjust the deformation path to be in a non-linear form. Some advanced systems feature real-time feedback controllers that can determine the path based on the deformed parameters, e.g., stress and strain [4].

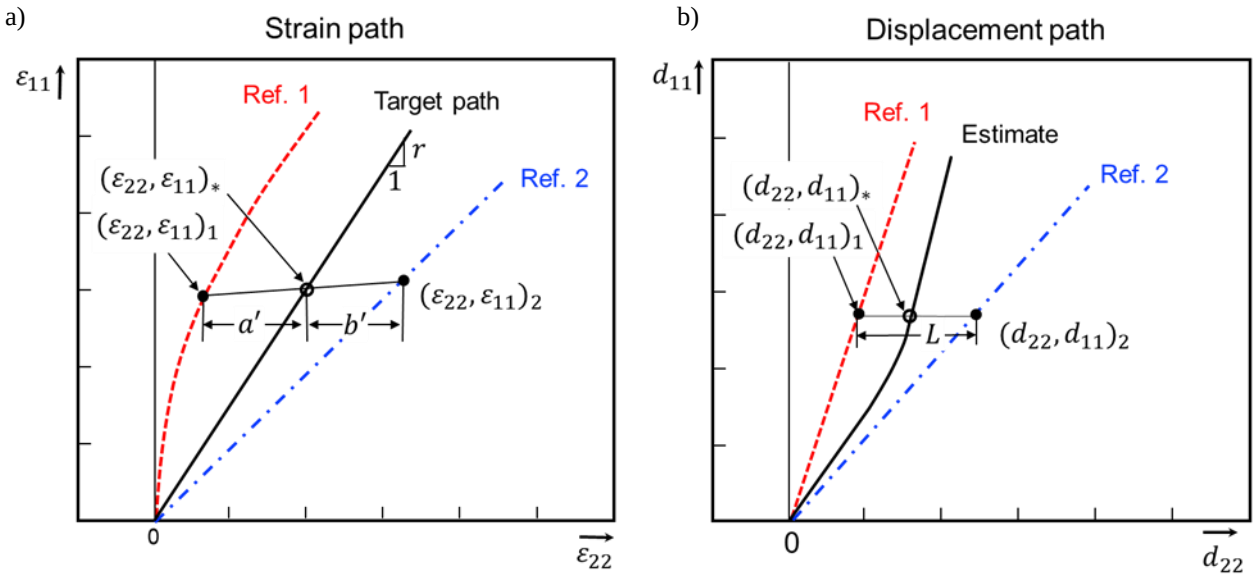

FIGURE 1.1: SCHEMATIC DESCRIPTION OF INTERPOLATION METHOD. a) DETERMINATION OF CORRECTION VARIABLES a' AND b' BASED ON TWO REFERENCE (REF) STRAIN CURVES (RED DASH AND BLUE DOT DASH) WITH TARGET RATIO (SOLID BLACK) IN BETWEEN. b) REFERENCE (REF) DISPLACEMENT PATHS AND RESULTING INTERPOLATED ESTIMATE FOR TARGET PATH.

2. INTERPOLATION METHOD

The interpolation method [1,2] requires two reference strain paths and a target linear strain path that will be the desired outcome. In this paper, initial reference curves were produced using linear input displacements in FE simulations (displacement ratios d_{11}: d_{22} of 2:2, 2:1, 2:0.5, 2:-0.4, and 2:-0.8). The target path must lie in between two selected reference curves as shown in Figure 1.1a). If a reference path crosses the target path, another reference curve may be used beginning at the increment of intersection for the remainder of the interpolation. The strain path is comprised of two components, i.e., the major and the minor direction strains, ε_{11} and ε_{22}, respectively. Accordingly, the major direction displacement d_{11}, which is held linear throughout the simulations, and the minor direction displacement d_{22}, that is adjusted systematically (Figure 1.1b), are obtained.

A calculation is performed using the strain data from the reference curves. In this calculation, a theoretical line is formulated to connect strain levels on the reference curves at each time increment of the FE simulation. This is shown in Figure 1.1a as connecting two points on the reference paths. Since the theoretical line is connecting the reference paths, it also passes through the target path. The intersection between them can be expressed in terms of the strain components in the reference paths and the target ratio, or linear slope of the target path, by:

$$(\varepsilon_{22})_* = \frac{\left[(\varepsilon_{11})_2 - \left[\frac{(\varepsilon_{11})_2 - (\varepsilon_{11})_1}{(\varepsilon_{22})_2 - (\varepsilon_{22})_1}\right] \times (\varepsilon_{11})_2\right]}{\left(r - \left[\frac{(\varepsilon_{11})_2 - (\varepsilon_{11})_1}{(\varepsilon_{22})_2 - (\varepsilon_{22})_1}\right]\right)} \quad (1)$$

where the subscripts 1, 2 and * refer to the left and right reference paths and a curve based on the target ratio 'r', respectively. Thus, the strain components at the intersection can be calculated as $(\varepsilon_{22},\varepsilon_{11})_* = (\varepsilon_{22}, r \cdot \varepsilon_{22})_*$. A relationship is then established in terms of correction variables a' and b' to quantify the normal distance from each reference curve to the target curve. The variables a' and b' are then used in a weighted average with the displacement values of the reference curves. A new displacement value is generated that will produce the target strain value at the corresponding increment. The relationship between the weighted average and the displacement path is:

$$(d_{22})_* = (d_{22})_1 + \frac{a'}{a'+b'}L \quad (2)$$

Figure 1.1b shows the visual interpretation of this relationship. This updated displacement path, when applied to the cruciform specimen in the FE simulations, will result in a linearized strain path that will be closer to the target strain ratio previously identified.

3. FINITE ELEMENT MODEL

The results presented in this paper are based on a FE model analyzed using Abaqus/Standard 2019. The cruciform specimen geometry was previously

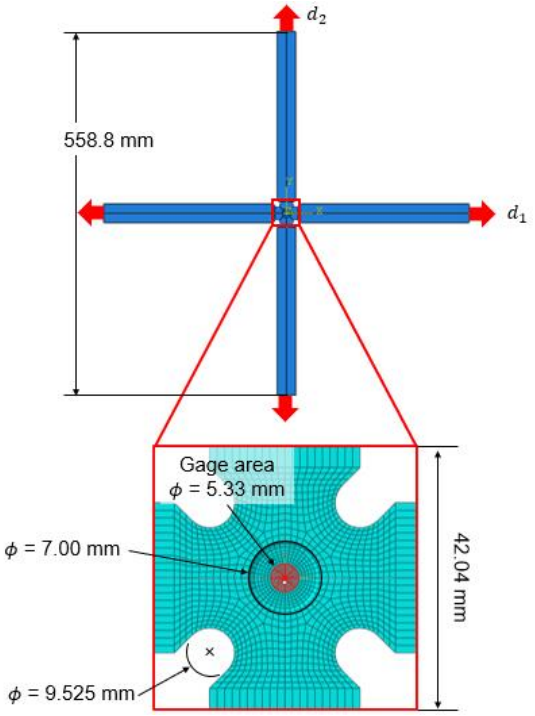

FIGURE 1.2 FE MODEL OF CRUCIFORM GEOMETRY

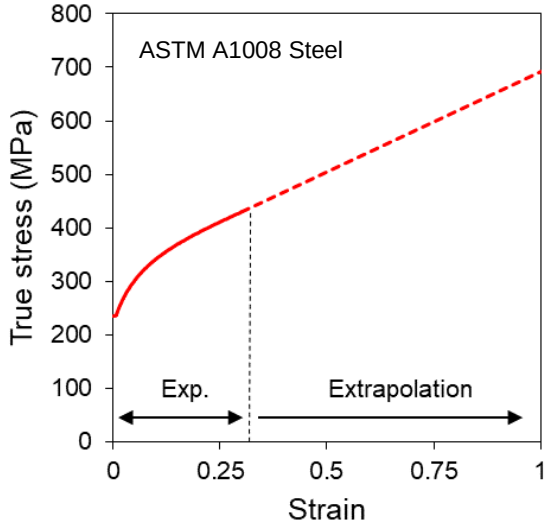

FIGURE 1.3 ASTM A1008 STEEL (EQUIVALENT TO AISI 1008 STEEL) STRESS-STRAIN CURVE FOR PLASTIC PROPERTIES.

optimized [5], features notched corners, and a reduced pocket thickness of 0.53mm from the 2.93mm original sheet thickness as seen in Figure 1.2. To save on computation time, only 1/8th of the full cruciform geometry was modeled with two-fold symmetries. Displacement boundary conditions along the x-and y-direction were applied at the end of the specimen arms with amplitudes at each time increment. The model was meshed using fully integrated hexahedral elements, with a higher concentration of elements in the pocket area where the deformation was concentrated. Four elements were assigned through the thickness direction. The strain data used for the interpolation was collected as an average of the center gauge area within the diameter of 5.33 mm (highlighted in red in Figure 1.2), which is roughly halfway between the center of the pocket and bottom of the fillet. The material used in this model was AISI 1008 steel with a Young's modulus of 210,000 MPa and Poisson's ratio of 0.3. The plastic material properties were previously determined experimentally (red solid) and extrapolated to a strain of 1 (red dash) [5] in Figure 1.3.

4. DOUBLE INTERPOLATION

Figure 4 shows an example of the input and output strain paths of the interpolation method. The selected target strain path in this paper is plane strain, i.e., $\varepsilon_{22}\approx 0$, which follows the y-axis in the strain plot. To begin the process, initial reference strain paths were generated for three linear displacement paths, i.e., $d_{11}:d_{22} = 2:-0.4$ (green dotted), $2:0.5$ (red dash), and $2:1$ (purple dot dash), by FE simulations for the cruciform model (Figure 1.4). The resulting strain paths from the simulations were non-linear and not close to the plane strain target. These strain paths then served as the reference curves in the interpolation process to produce a linear strain path for a plane strain condition.

Since the strain path of $2:0.5$ (red dash) crosses the target plane strain path (black solid), the interpolation method was applied in two parts with different sets of

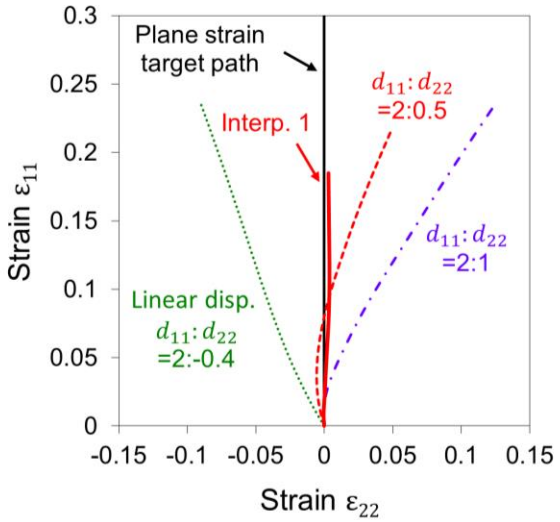

FIGURE 1.4 RESULTS OF INITIAL INTERPOLATION OF PLANE STRAIN PATH (FROM RED DASH TO RED SOLID LINE) USING PAIRS OF THE THREE REFERENCE CURVES SHOWN.

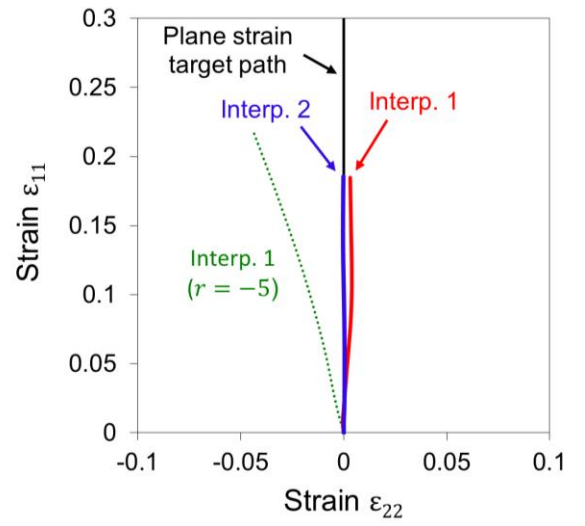

FIGURE 1.6 RESULTS OF DOUBLE INTERPOLATION (BLUE SOLID LINE) COMPARED TO SINGLE INTERPOLATION (RED SOLID LINE) AND TARGET PATH (BLACK SOLID LINE).

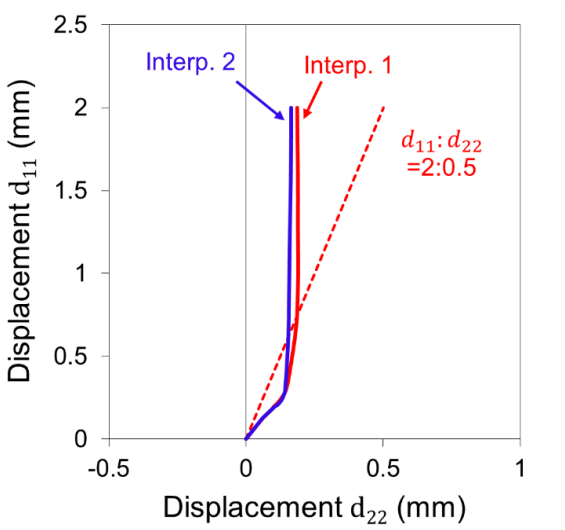

FIGURE 1.5 DISPLACEMENT PATH COMPARISON OF DOUBLE INTERPOLATION (BLUE SOLID LINE), SINGLE INTERPOLATION (RED SOLID LINE), AND LINEAR (RED DASH LINE).

reference curves. For the first part, before the strain path of $2{:}\,0.5$ intersects the plane strain target, the strain paths of $2{:}\,0.5$ and $2{:}\,1$ were used for the interpolation. Then, for the second part, curves $2{:}-0.4$ and $2{:}\,0.5$ were used.

The result of the interpolation is shown as the solid red line in Figure 1.4. While the path shows increased linearity and is close to the targeted path, there is a visible difference with the target due to the non-linearity at the beginning. Thus, it is proposed to interpolate a second time, named as double interpolation here, to get even closer to the target. In this second iteration, the result of the first interpolation (red solid in Figure 1.4) was used as one of the reference curves instead of the $2{:}\,1$ path.

Figure 1.5 shows the result of the second interpolation (blue solid) with two references (green dotted and red solid) and target path (black solid). It should be noted that the strain path for $r = -5$ (strain ratio $2{:}-0.4$) was also interpolated during the first interpolation and the updated path (green dotted in Figure 1.5) was used to improve the result in the second interpolation iteration plane strain path. Compared to the single interpolation, the result of double interpolation shows much improved linearity and is closer to the target plane strain path.

Figure 1.6 shows the corresponding displacement paths that were obtained from this interpolation progression. The red dash line represents the initial linear displacement path of $2{:}\,0.5$, the red and blue solid lines are the results of the single and double interpolations (first and second iterations), respectively. These displacement paths represent a progression towards approaching the desired linear plane strain path.

5. CONCLUSION

Through a progression from linear input displacement to single and double interpolated outputs, it has been shown that the interpolation method can achieve results closer to the target path, in this case a plane strain forming condition. This result has great implications to biaxial tension testing for users to produce a desired strain path through the displacement control. Future work will include experiments to validate the success of this method by applying the optimized displacement path into the experimental set up. The strain will be measured by a surface 3D stereo digital image correlation (stereo-DIC) system and compared to the simulated results.

ACKNOWLEDGEMENTS

Support from the National Institute of Standards and Technology, through the Summer Undergraduate Research Fellowship (SURF) program, and funding for the NH BioMade Project from the U.S. National Science Foundation EPSCoR award (#1757371) are gratefully acknowledged.

DISCLAIMER

Certain commercial software, equipment, or materials are identified in this paper in order to specify the experimental procedure adequately. Such identification is not intended to imply recommendation or endorsement by the National Institute of Standards and Technology, nor is it intended to imply that the software, materials, or equipment identified are necessarily the best available for the purpose.

REFERENCES

[1] Hoffman, J., Banerjee, D., Iadicola, M., "Determination of Strain Path Envelope in an Optimized Biaxial Cruciform Specimen of AISI 1008 Steel under Linear, Bilinear, and Nonlinear Strain Paths", *The Materials Society Conference* 2022

[2] Banerjee, Dilip, Mark Iadicola, Adam Creuziger, and Timothy Foecke. "An experimental and numerical study of deformation behavior of steels in biaxial tensile tests." *In TMS 2015 144th Annual Meeting & Exhibition*, pp. 279-288. Springer, Cham, 2015.

[3] Deng, N., Kuwabara, T., Korkolis, Y.P., "Cruciform Specimen Design and Verification for Constitutive Identification of Anisotropic Sheets," *Experimental Mechanics*, 55, 6, 1005-1022, 2015

[4] Yanaga, D., Kuwabara, T., Uema, N., Asano, M. "Material modeling of 6000 series aluminum alloy sheets with different density cube textures and effect on the accuracy of finite element simulation." *International Journal of Solids and Structures*, 49 25, 3488-3495, 2012

[5] Creuziger, A., Iadicola, M., Foecke, T., Rust, E., and Banerjee, D., 2017, "Insights into Cruciform Sample Design," *JOM*, 69(5), pp. 902-906.

CHAPTER 2

INTERPOLATION TO ACHIEVE CONSTANT STRESS STATES FOR SS304L CRUCIFORM SPECIMEN

1. INTRODUCTION

Sheet metal forming is an important process in modern manufacturing practices, such as in the biomedical and automotive industries, producing high quantities of parts with consistent quality and at a low cost. During forming processes, the material experiences complicated deformations under multi-axial stress states. This creates a challenge to develop appropriate constitutive models to capture the unique material behavior observed in sheet metal forming processes. Another complexity, which can be incorporated into modeling efforts if the behavior is well understood from material testing, is plastic deformation induced microstructural changes. For example, austenitic stainless steels experience deformation-induced α'-martensite phase transformation, which has a significant impact on the mechanical properties of the formed part. A study conducted by Fahr found that ductility and strength are enhanced with the formation of martensite (Fahr, 1971), which are desirable in formed parts in general.

Many material models have been developed to define the transformation kinetics of martensite in steels. To date, deformation induced martensite transformation has been found to depend on equivalent plastic strain level, stress state, strain rate and temperature (Beese and Mohr, 2011; Olson and Cohen, 1975 Stringfellow et al. 1992; Geijselaers et al., 2013). Olson and Cohen developed a model in 1975 which relates the deformation induced martensite volume fraction to equivalent plastic strain and temperature (Olson and Cohen, 1975). Stringfellow et al. expanded this model to include a dependance on the stress state during deformation, via stress triaxiality (Stringfellow et al. 1992). More recently, Beese and Mohr revisited the model and integrated the Lode angle parameter to account for the martensite transformation induced by both the normal

and shear stresses (Beese and Mohr, 2011). Each of the models showed improved experimental agreement as new parameters were introduced based on physical phenomena exhibited in experimental results.

Validation of such models can require extensive experimental efforts due to the stress state dependance of the transformation kinetics. Figure 2.1 depicts how the martensite transformation changes significantly with different stress states, which are equivalent to the stress ratio.

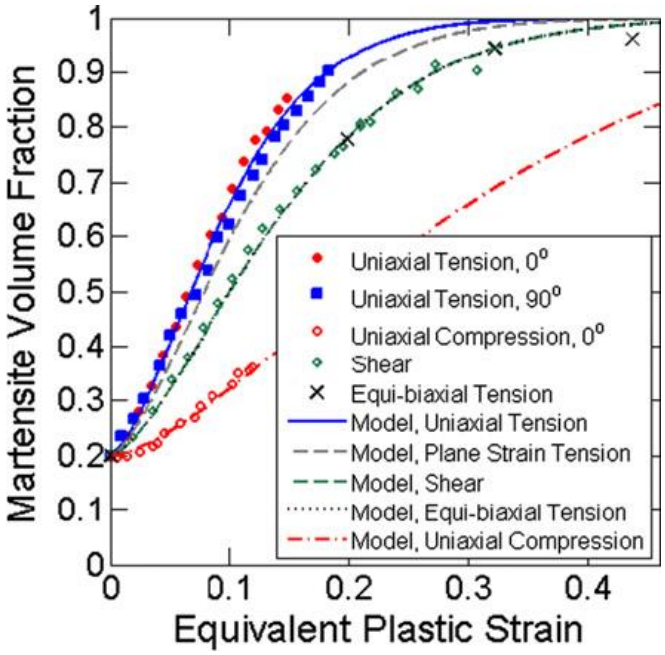

Figure 2.1. Varied martensite transformation kinetics for various stress states from uniaxial tension to uniaxial compression. (Beese and Mohr, 2011)

Each of the stress states plotted in Figure 2.1 can be achieved using different experimental setups and specimen geometries. For uniaxial loading, both tension and compression experiments can utilize ASTM-E8 or similar type specimens on a universal testing machine (ASTM E8 M, 2016). Specimens in compression may require an anti-

buckling device to suppress out-of-plane deformation. The device must allow ample view of the specimen during testing for optical data collection methods, such as digital image correlation (DIC), or mechanical data collection methods such as a foil strain gage or extensometer.

Simple shear stress states can be achieved using various experimental methods depending on specimen geometries. Single or double-notched type specimen can be tested using a uniaxial loading machine (Beese and Mohr, 2011, 2012). The axial loading is transformed into simple shear by the specimen geometry in the deformation region. In-plane torsion is also a method for simple shear testing that can be applied to sheet metals (Yin et al., 2013). In-plane torsion induces shear by applying rotational deformation to a fixed disk shaped specimen.

An equibiaxial tension stress state can be attained using a punch or hydraulic bulge test (Beese and Mohr, 2011; Wang, Xu, and Shou, 2016; Nikhare et al., 2017). Both testing methods symmetrically deform the specimens in equibiaxial tension, however, it is necessary to account for friction between the tools and specimen in the punch test (Wang, Xu, and Shou, 2016). DIC can be used for full-field strain data collection in both testing methods. A ferritescope can be utilized to measure the martensite transformation as well as x-ray diffraction and electron back-scatter diffraction (Talonen et al., 2004). Although past research using different experimental setups and specimen geometries showed successful analysis of stress states, the desparities in experimental procedure may involve high potential for uncontrolled variation between each of the experiments.

Alternatively, in-plane biaxial cruciform testing is a flexible material testing method to achieve numerous stress states using one loading frame and one specimen geometry.

The specimen has a cross shape with four arms, which are deformed orthogonally, and material behavior is measured in the center gauge area. Biaxial testing frames consist of four hydraulic or mechanical actuators, mechanical grips to secure the specimen, and a control system to apply the prescribed deformation path (Hannon and Tiernan, 2008; Deng et al., 2015; Hanabusa et al., 2010, 2013; Zhao et al., 2019). Force and displacement are common control inputs, but they may not produce a desired stress state. More advanced systems, incorporating, e.g., DIC, to feedback the deformation to the controller in real-time (Yanaga et al., 2012), have been developed, but they are complex and expensive in general.

In past research, geometric variations of the cruciform specimen geometry have been studied to improve the testing performance (Banerjee et al., 2015). They stated that various design parameters can be considered based on the ISO standard geometry (ISO 16842, 2014) depending on user's purpose. Examples include, to increase the deformation achievable in the cruciform specimen; to enlarge uniform deformation in the gauge area; to concentrate the deformation to induce the fracture at a desired location, etc. The ISO standard specimen only reaches gauge area strains up to 25% of the fracture strain (Nasdala and Husni, 2020; ISO 16842, 2014). Hannon and Tiernan (2007) summarized key geometric features that can be implemented individually or combined to achieve higher deformation levels in biaxially loaded specimens. A reduced pocket thickness in the center gauge area of the specimen caused deformation to be concentrated in the gauge section rather than the specimen arms (Deng et al., 2015; Hou et al., 2018; Zhao et al., 2019). A circular notch in the corners of the specimen arms and thin slots machined along the specimen arm lengths can reduce stress concentrations

(Gerke et al., 2017; Giannella et al., 2019) and increase the deformation in the gauge region of the specimen (Deng et al., 2015; ISO 16842, 2014; Kuwabara et al., 1998.) Each of these features allows for higher stress and strain to be achieved; however, they will result in non-uniform deformation regions and thus non-constant stress states. Since linear stress paths indicate constant stress triaxialities and constant stress states and cannot be controlled through geometric variations, there is a need to derive non-linear displacement paths to produce linear stress paths.

In this chapter, an interpolation method to achieve linear stress paths is implemented on a SS304L cruciform specimen. The predicted mechanical response to the applied interpolated displacements is modeled numerically using finite element (FE) software. Section 2 will describe the interpolation algorithm and the iterative nature of the method. Section 3 will detail the FE model used to simulate the displacement paths produced, as well as detail the interpolation of the pure shear stress state. Final simulated displacement paths and their corresponding stress paths and stress triaxiality will be presented for five individual stress states. Section 4 will summarize the findings and discuss future experimental plans.

2. REVIEW OF INTERPOLATION METHOD

In this work, the interpolation method is utilized to derive non-linear displacement paths to produce linear stress paths, equivalently constant stress triaxialities, in the gauge section of a cruciform specimen. For each stress path of interest, the interpolation method requires two or more stress reference curves and their corresponding displacement paths (see chapter 1). These paths are adjacent to each side of the target path with the linear stress ratio $m = \frac{\sigma_{11}}{\sigma_{22}}$ when the 11-direction is assumed to be the major loading direction.

Initial reference stress curves are typically produced by applying linear input displacements to FE simulations (displacement ratios $d_{11}{:}\,d_{22}$) and collecting the respective stress data from the center of the cruciform model. The reference curves must lie to the left and right of the target path, which can be seen in Figure 2.2B. If a reference path intersects the target path, another reference path may be used beginning at the increment where the original path and target path cross. The normal stress path is comprised of two components in the major and the minor direction, i.e., σ_{11} and σ_{22}, respectively. Thus, the corresponding displacement path is also composed of d_{11} and d_{22}. Only d_{22} is adjusted at each increment systematically through interpolation to linearize the stress path.

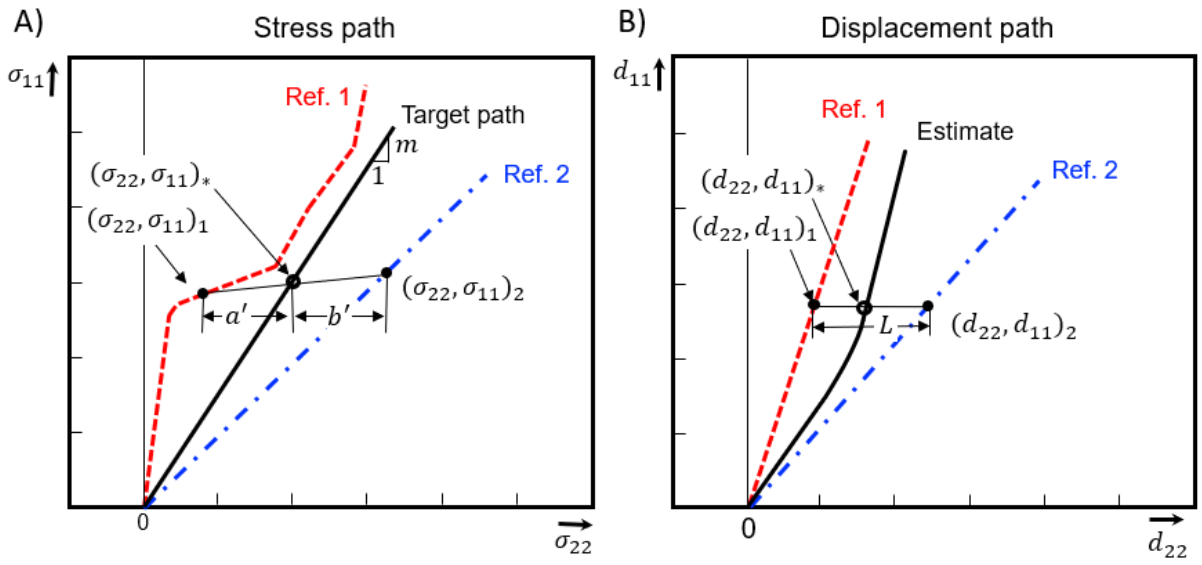

Figure 2.2 Schematic of interpolation method. A) Determination of correction variables a' and b' based on two reference (Ref.) curves (red dash and blue dot-dash) with target path (solid black) in between. B) Reference (Ref.) displacement paths and resulting interpolated estimate displacement path for target normal stress path.

Following the collection of the appropriate reference data, a calculation is performed at each increment of the simulation. In Figure 2.2A, an interpolation line is depicted which connects the stress values on the reference curves at a specified time increment in the simulation and passes through the target path. This interpolation line is described by an equation which defines the stress value on the target path in terms of the stress values in the reference paths as follows:

$$(\sigma_{22})_* = \frac{\left|(\sigma_{11})_2 - \left|\frac{(\sigma_{11})_2 - (\sigma_{11})_1}{(\sigma_{22})_2 - (\sigma_{22})_1}\right| \times (\sigma_{11})_2\right|}{\left(m - \left|\frac{(\sigma_{11})_2 - (\sigma_{11})_1}{(\sigma_{22})_2 - (\sigma_{22})_1}\right|\right)} \quad (1)$$

The subscripts 1, 2, and * correspond to the left and right references and the target path, respectively. Further, the stress components along the target path can be calculated as $(\sigma_{22}, \sigma_{11})_* = (\sigma_{22}, m \cdot \sigma_{22})_*$. Correction variables a' and b' are now calculated which represent the distance from each reference path to the target path. Then, the updated displacement path can be calculated by using a weighted average of the correction variables with the reference displacement paths. The equation to describe the relationship between the correction variables and the interpolated displacement path is:

$$(d_{22})_* = (d_{22})_1 + \frac{a'}{a' + b'} L \quad (2)$$

This is visually represented in Figure 2.2B and is comparable to the “lever rule” or “reverse arm rule” in chemical phase transformation (Adewumi, 2020). The lever rule

allows for the composition of a two phase mixture to be determined using a similar weighted average as in the displacement calculation. The displacement calculation procedure is performed for each increment throughout the simulation until a complete displacement path is produced.

To achieve an acceptable linear stress path that agrees with the target ratio, it is necessary to perform multiple iterations of the interpolation calculation. New iterations of interpolation will achieve improved agreement with the identified target path by replacing one or both reference curves with the stress and displacement results of the previous iteration of interpolation. Employing the previously interpolated results limits the new interpolated displacement path since the estimate target displacement path will always fall between the displacement paths of the reference curves. Each iteration will generate a displacement path that results in a stress path closer to the target. This is represented schematically in Figure 2.3. Figure 2.3A depicts the progression of stress path moving closer to the target with each iteration. Figure 2.3B illustrates that the displacement path shifts with each iteration, exhibiting less change as more iterations are performed and the stress path approaches the target.

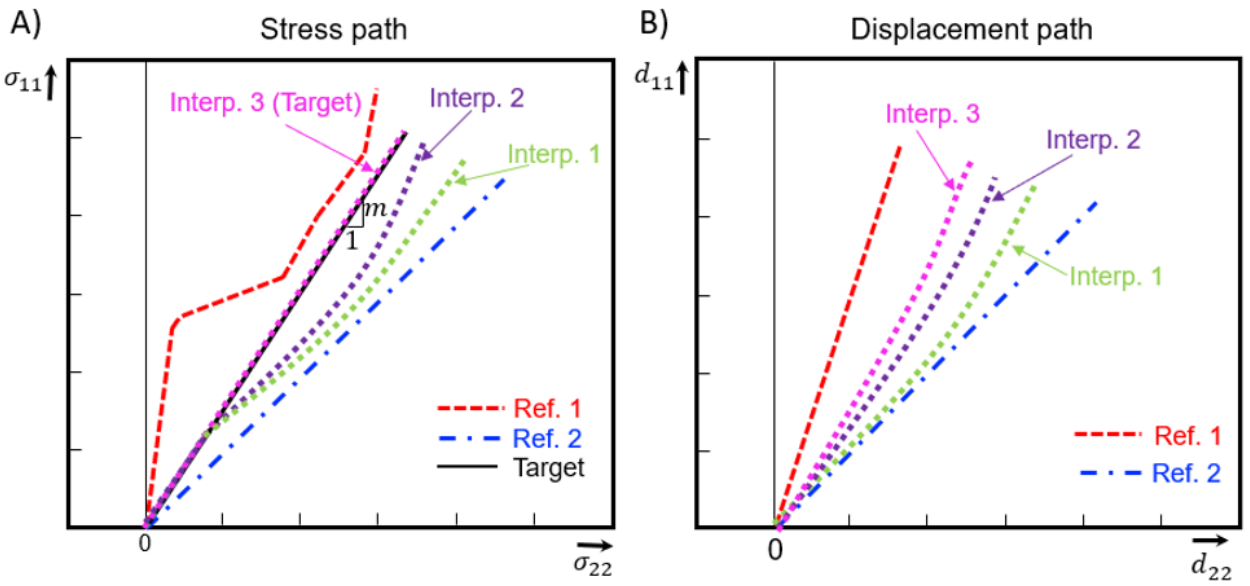

Figure 2.3 Schematic of iterative progression of interpolation method. A) Successive iterations of the stress interpolation approaching the target path. B) Displacement paths of successive iterations shifting with each interpolation iteration.

Iterations of interpolation continue until acceptable agreement with the target path is achieved. This termination has been chosen numerically to be a parameter related to the stress triaxiality observed in the center of the specimen. Stress triaxiality is described by the first invariant of the Cauchy stress tensor, commonly recognized as the mean hydrostatic pressure (σ_m), divided by the second invariant of the deviatoric stress tensor, commonly described as the equivalent stress ($\bar{\sigma}$). The equation for stress triaxiality is written:

$$\eta = \frac{\sigma_m}{\bar{\sigma}} \tag{3}$$

The stress triaxiality is calculated for each iteration of the simulation and plotted as a function of plastic equivalent strain. The target stress triaxiality is calculated using the target stress ratio 'm' and remains constant through the entire applied deformation. The difference between the calculated target and simulated stress triaxiality values from the interpolated displacement path is computed using the sum of the square error at each increment of the simulation through the entire displacment history. The equation to calculate the sum of the square error is:

$$SSE = \sum_{i=1}^{n} (\eta_i - \hat{\eta}_i)^2 \tag{4}$$

Where the sum of the square error is denoted SSE, i is the increment of the simulation where there are n total increments, η_i is the simulated stress triaxiality, and $\hat{\eta}_i$ is the target stress triaixiality. The criteria in this paper used to determine the end of the interpolation progression is when the sum of the square error is below 0.13 and the difference in sum of square error between successive iterations is below 0.03 These parameters represent a low error compared to the target stress triaxiality as well as a low potential for improvement with continued iterations. These values were chosen through analysis of the simulation results to establish a representative termination criterion.

3. LINEARIZATION OF STRESS PATH USING INVERSE METHOD

3.1 FINITE ELEMENT MODEL

Stress results for each interpolated displacement were generated using FE simulations in Abaqus/Standard 2019. The cruciform geometry used in the simulations was based on the geometry from Mamros et al (Mamros et al., 2022). Mamros' geometry was optimized for plasticity characterization of SS316L, however the uniaxial stress-strain

curves of SS304L and SS316L agree well at 20°C. A geometry based on Mamros' could be implemented for SS304L and achieve similar mechanical performance, e.g. high strain levels. The geometry dimensions are shown in Figure 2.4. Key geometric features include notched corners of 10 mm diameter and a 50% reduced pocket thickness in the center of specimen.

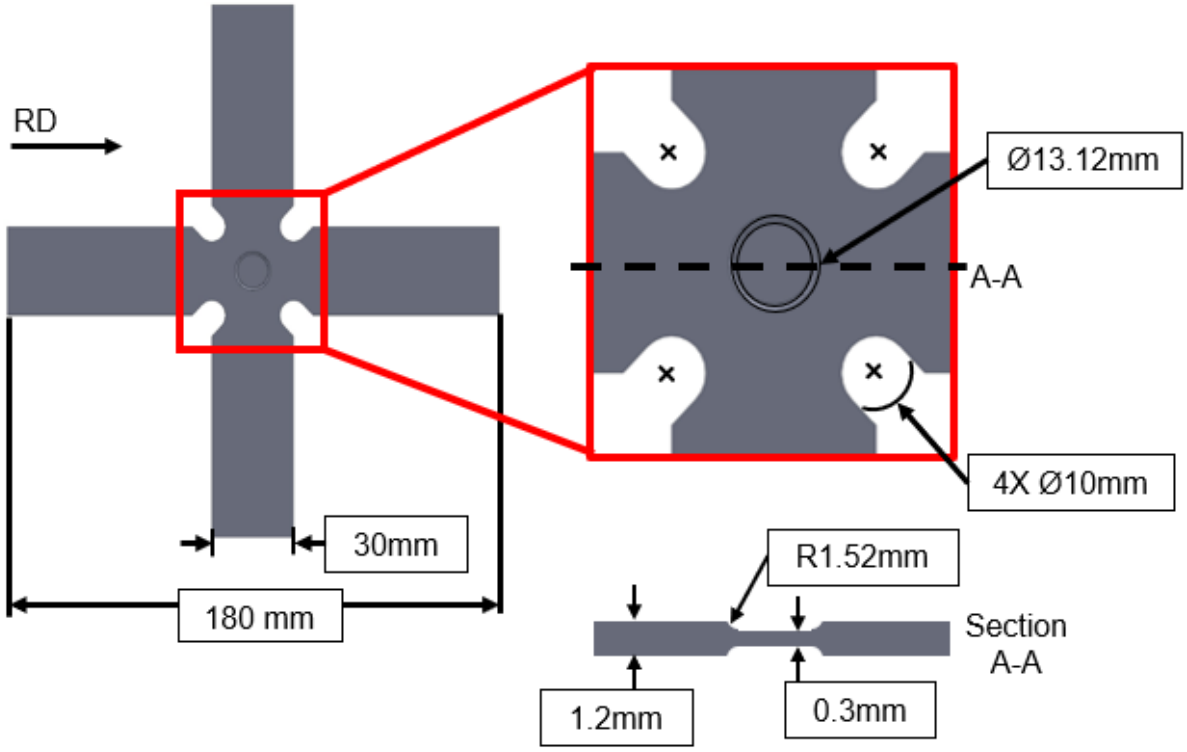

Figure 2.4 Cruciform Geometry

These features will reduce stress concentrations in the corners of the specimen, localize deformation in the center, and allow for strain levels higher than the 25% achieved by the ISO standard specimen (ISO 16842, 2014).

The material used in this study is a low carbon fully austenitic stainless steel 304 (SS304L). The material was chosen due to its prevalence in sheet metal forming applications and it has been shown to have high values of deformation induced phase

transformation (Liu, 2016). A user defined material subroutine (UMAT) implemented with an isotropic hardening, i.e., Hockett-Sherby, and a non-quadratic anisotropic yield function, i.e., YLD2004-18p, for SS304L was applied to the simulation (Hockett and Sherby, 1975). The Hockett-Sherby parameters were determined through a series of uniaxial tension tests conducted at 20°C. The parameters are listed in table 2.1 below:

Table 2.1 Experimentally determined Hockett-Sherby model parameters.

Parameter	Value
σ_0	297.37 (MPa)
H	2137.96 (MPa)
N	1.12
m	0.93

The Hockett-Sherby model is:

$$\bar{\sigma} = H - (H - \sigma_0) \cdot exp(-N \cdot \bar{\varepsilon}^m) \tag{4}$$

Yld2004-18p function is as follows:

$$\begin{aligned}\phi = \phi(\tilde{\boldsymbol{S}}', \tilde{\boldsymbol{S}}'') = &\left|\tilde{S}_1' - \tilde{S}_1''\right|^a + \left|\tilde{S}_1' - \tilde{S}_2''\right|^a + \left|\tilde{S}_1' - \tilde{S}_3''\right|^a \\ &+\left|\tilde{S}_2' - \tilde{S}_1''\right|^a + \left|\tilde{S}_2' - \tilde{S}_2''\right|^a + \left|\tilde{S}_2' - \tilde{S}_3''\right|^a \\ &+\left|\tilde{S}_3' - \tilde{S}_1''\right|^a + \left|\tilde{S}_3' - \tilde{S}_3''\right|^a + \left|\tilde{S}_3' - \tilde{S}_3''\right|^a = 4\bar{\sigma}^a\end{aligned} \tag{5}$$

$\tilde{S}_i'$ and $\tilde{S}_i''$ are principal values of linearly transformed stress tensors, i.e., $\tilde{\boldsymbol{S}}'$ and $\tilde{\boldsymbol{S}}''$, and an exponent a (Barlat et. al., 2005).

1/8th of the total specimen geometry was modeled in the simulation, taking advantage of the three symmetry planes, and reducing computation time. The model

mesh is comprised of reduced integration point hexahedral elements (C3D8R). A higher concentration of elements was assigned in the pocket of the cruciform compared to the arms, as this is the region of interest. Four elements were assigned in the half thickness direction, then mesh seeds were assigned to edges of each partition. Seeds are markers that are placed along the edges of a region to specify the target mesh density in that region. Both the mesh density along the boundary of the region and the mesh density in the interior of the region are determined by the seeds along the edges of the region. Applying edge seeds allowed for enhanced control of the mesh compared to global seeding and ensured appropriate mesh symmetry and element resolution. The 1/8th model mesh is composed of 5,828 elements. Images of the model mesh are displayed in Figure 2.5.

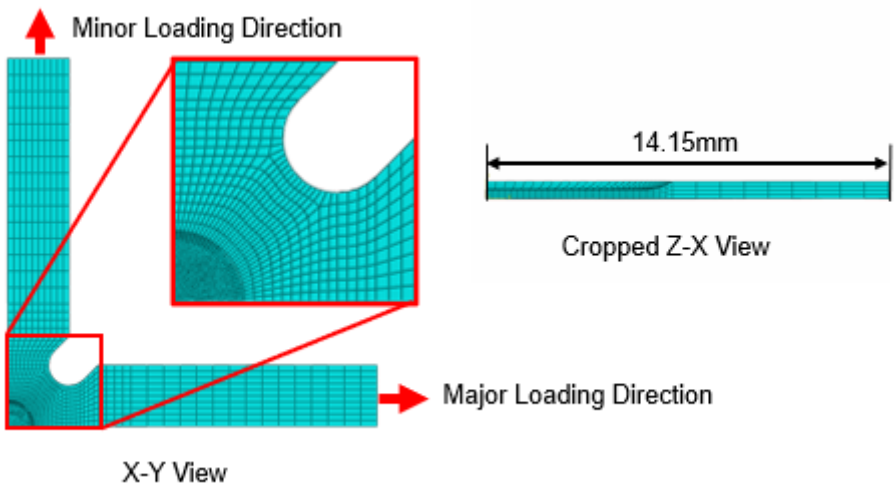

Figure 2.5 1/8th cruciform model

Reference points were generated at 15 mm from the end of the cruciform arms and coupled kinematically to the end face of the specimen arms to simplify data

extraction. Displacements with amplitudes were applied via x- and y-direction boundary conditions to the reference points. All translational and rotational degrees of freedom for the x-arm displacement boundary condition were restricted except for the x-direction. The same restrictions applied for the y-arm displacement boundary condition, except for the y-direction accordingly. Stress in the 11 (x-direction) and 22 (y-direction) were output from the surface center element integration point at each of the time steps. The surface element was chosen because future experimental data will also be captured from the surface of the specimen. In addition to the stress components, pressure and equivalent stress were extracted to calculate the stress triaxiality at the same location.

3.2 RESULTS

In this paper, the results are presented for five interpolated stress paths which represent five unique stress states. The stress states were chosen to span the entire stress envelope. The stress ratios of the five chosen stress paths are as follows: 1:-1 (pure shear), 2:-1, 1:0 (uniaxial tension), 2:1, 1:1 (equibiaxial tension). The five target stress paths can be seen in Figure 2.6.

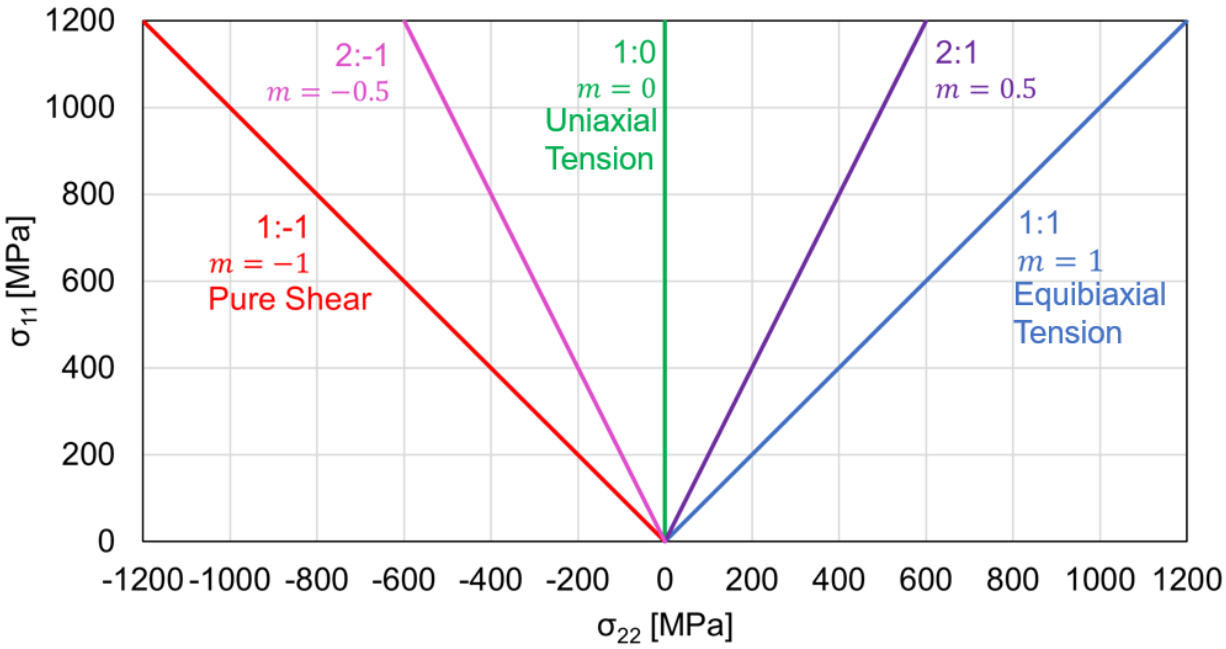

Figure 2.6 Five target linear stress curves labeled by their stress ratio $(\sigma_{11}:\sigma_{22})$ and target ratio m.

Prior to interpolation, nine reference curves were generated by linear displacement paths. Nine total linear reference paths were needed to ensure a left and right reference curve for each of the identified target paths. The stress components were collected from the center element at each of the increments. Figure 2.7A depicts the reference stress paths produced by the linear displacement paths in Figure 2.7B. It should be further noted that the stress paths from the linear displacement paths are highly non-linear compared to the targeted stress paths. Thus, the need for a method to develop displacement paths to achieve desired linear stress is emphasized.

The interpolation process was applied to each of the five stress states individually. Starting with the pure shear stress state ($\sigma_{11}:\sigma_{22}$,=1:-1) a combination of four reference curves ($d_{11}:d_{22}$=6:-7, 1:-1, 3:-2, 2:-1) from linear displacement paths were utilized in the

first iteration of interpolation. Multiple reference curves were required due to the intersections of the $d_{11}:d_{22}$ =1:-1 and 3:-2 reference curves with the $\sigma_{11}:\sigma_{22}$=1:-1 target curve. The $d_{11}:d_{22}$=1:-1 reference curve was used before the intersection increment with the $\sigma_{11}:\sigma_{22}$ =1:-1 target curve, around (-450,450) MPa. Then, from the intersection increment, $d_{11}:d_{22}$=3:-2 reference curve was used until the second intersection increment with the $\sigma_{11}:\sigma_{22}$=1:-1 target path, around (-650,650) MPa. The $d_{11}:d_{22}$=2:-1 reference curve was used for the remaining increments.

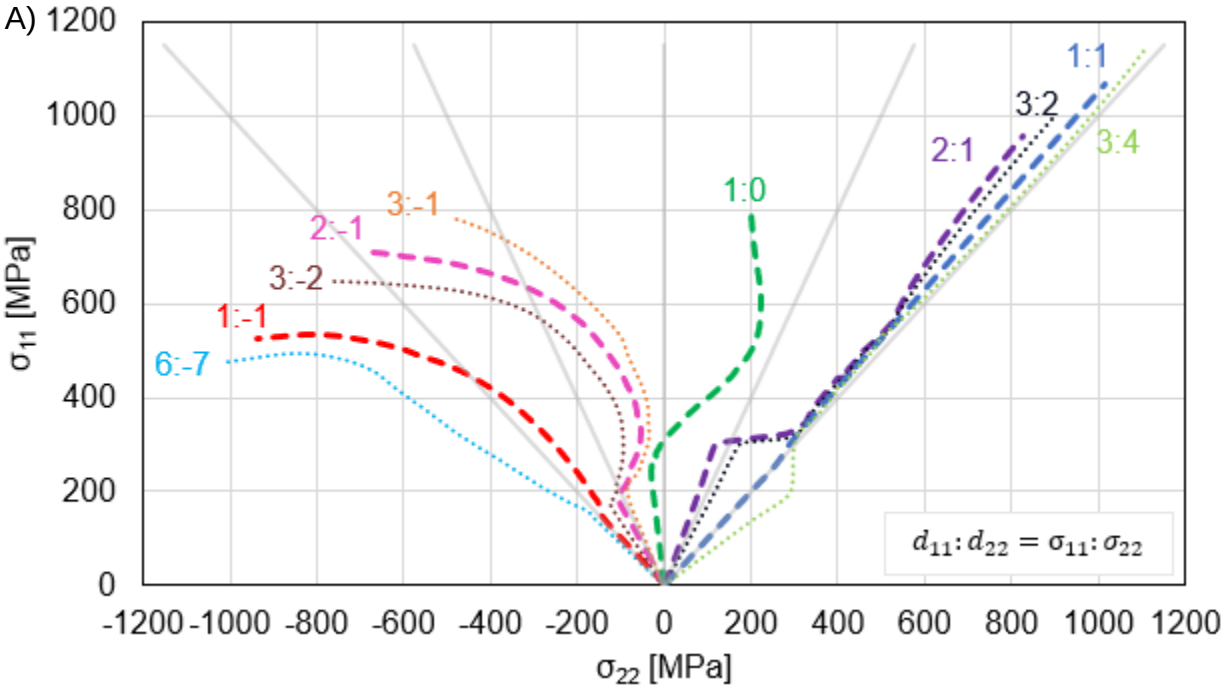

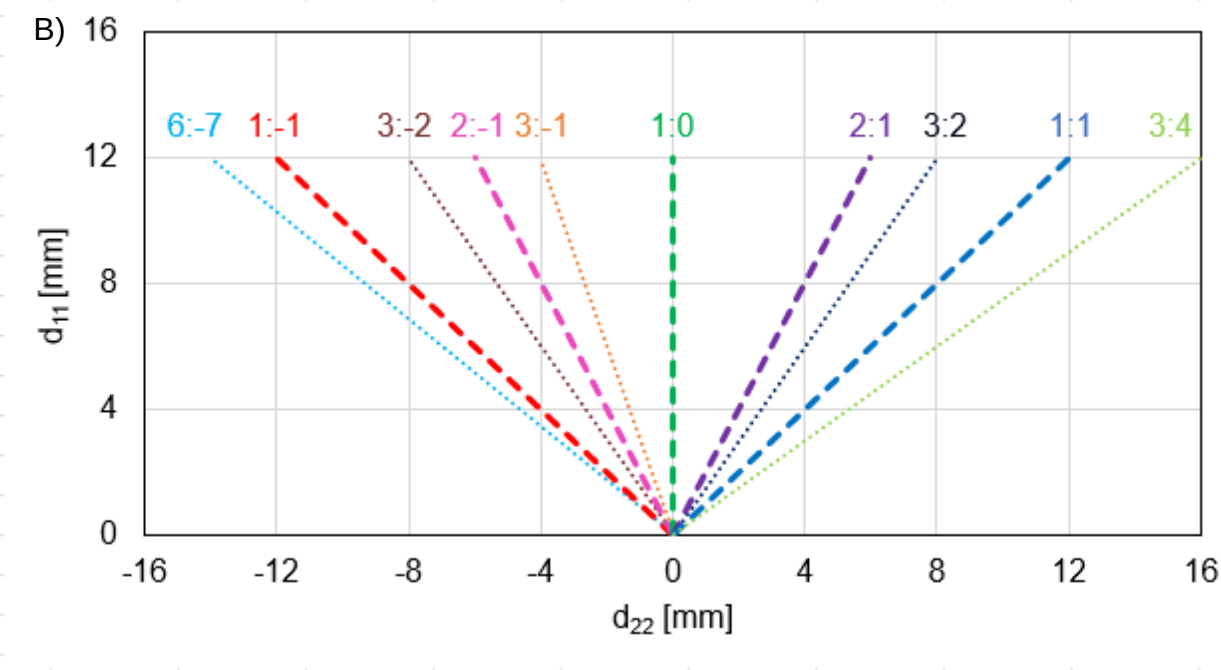

Figure 2.7 A) Nine stress reference curves to be used for interpolation of five stress states. Dash line represents linear input displacement ratio equal to targeted linear stress ratio. Gray solid lines are targeted linear stress for comparison. Dotted line are additional reference curves simulated to be sure each target curve will have a left and right reference path. B) Linear input displacements for reference curves.

The interpolated displacement path is a sequence of the interpolations preformed using the three combinations of reference paths discussed. The resulting first iteration interpolated displacement path is shown as the solid dark blue line in Figure 2.8B. The value in the parenthesis of the legend entry indicates the iteration of interpolation, with zero representing the linear input displacement with a displacement ratio equal to the target stress ratio. The interpolated displacement path is then applied to the FE model to extract the updated stress path (solid dark blue line) as seen in Figure 2.8A. The stress path is much closer to the identified target path than any of the original reference curves.

However, divergence is observed starting at (-400,400) MPa increasing throughout the remainder of the path.

A)

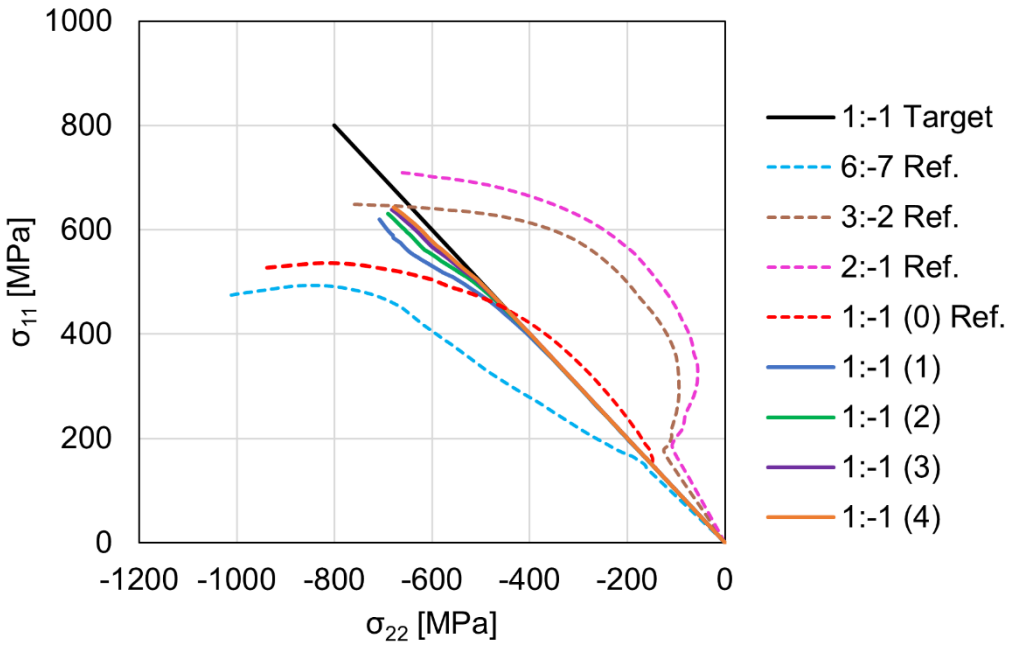

B)

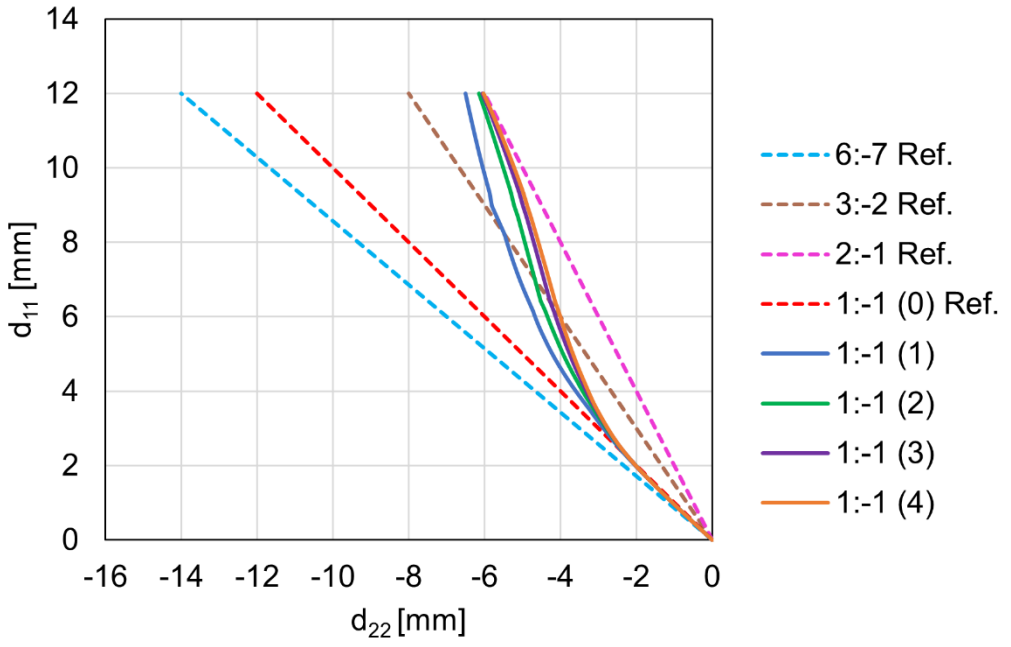

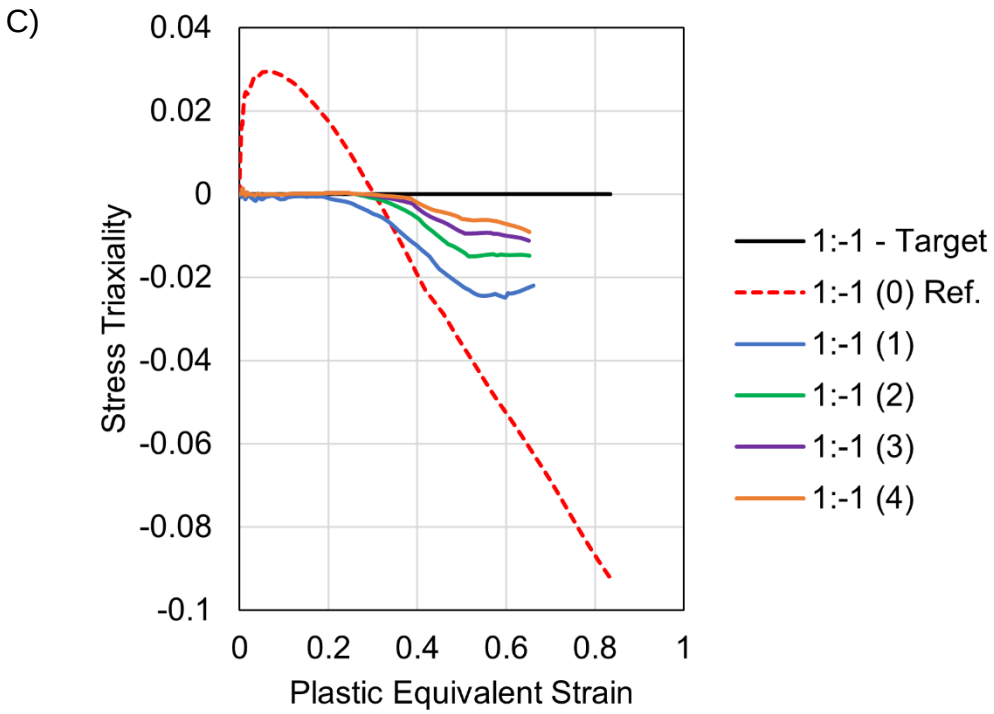

Figure 2.8 Progression of pure shear (1:-1) stress interpolation. A) Reference (ref.) (dotted) and interpolated (solid) stress paths extracted from simulations. B) Reference (ref.) (dotted) and interpolated (solid) displacement paths. C) Stress triaxiality of linear input displacement equal to target stress ratio (red dash, Interpolation 0 or Ref.) and interpolated stress triaxiality (solid), shown as a progression towards the target value (black solid).

The divergence is quantified by analyzing the stress triaxiality. The sum of the square error between the target and simulated stress triaxiality is calculated following each iteration of interpolation. This value is compared to the established termination criteria (see section 2). In Figure 2.8C, both the target and simulated stress triaxialities are plotted as a function of plastic equivalent strain. Notice that the target stress triaxiality is constant, meaning a constant stress state of pure shear is assumed for the duration.

The divergence of the interpolated (blue solid) stress path and the target (black solid) is also apparent in the respective stress triaxiality paths in Figure 2.8C. This difference is quantified by the sum of the square error in Table 2.1. The calculated sum of square error for the first iteration of interpolation is 4.096, significantly higher than the termination criteria of 0.13. Thus, more iterations of interpolation must be performed.

Table 2.2 Progression of 1:-1 interpolation termination criteria over successive iterations up to 65% plastic equivalent strain.

Iteration	Sum Sq. Error	Difference in Sum Sq. Error
0	4.096	
1	0.275	3.821
2	0.102	0.173
3	0.043	0.059
4	0.021	0.023

In the next iterations of interpolation, the left reference curve is replaced by the interpolated stress path. The right reference curve remains comprised of the 1:-1, 3:-2 and 2:-1 linear input reference curves. The second iteration of interpolated displacement path is shown in Figure 2.8B as the green solid line. This second iteration displacement path is shifted to the right compared to the first iteration, representing a correction from the first interpolation in which the stress path was diverging to the left from the target path. The same trend can be seen visually in the stress triaxiality in Figure 2.8C and numerically in Table 2.1. The sum of square error value has now dropped below 0.13 for the second iteration, however the difference in sum of square error between the first and second iteration is greater than 0.03, thus the second termination criteria is not satisfied. This

indicates there is potential for further improvement with continued iterations. The interpolation process repeats for a total of four iterations before a result is produced which satisfies both terminating criteria. The fourth iteration has a sum of the square error of 0.021 and the difference in the sum of the square error of 0.023. The fourth iteration is depicted in Figure 2.8 A, B, and C, as the solid orange line. When compared visually to the linear input displacement (interpolation 0) and the other successive iterations, there is a clear progression toward the defined target path. The fourth iteration of interpolated displacement is determined to produce a reasonable linear stress path with agreement to the target path.

A similar interpolation process is repeated for the remaining stress states. Each interpolation begins with a set of reference curves and progresses until the termination criteria is satisfied (See Appendix A). As the stress states are successfully interpolated, the resulting stress and displacement paths are also used as reference curves for the interpolation of the adjacent stress states. This improves the efficiency of the interpolation process, as the previously interpolated displacement paths are closer to the desired displacement than the linear reference displacement paths. The resulting stress paths, for each of the five stress states, produced by the interpolated displacement is shown in Figure 2.9. The gray curves are the target stress paths for comparison. The number in parenthesis beside each curve entry indicates the number of interpolation iterations required to produce the displayed path and accordingly achieve the established terminating criteria.

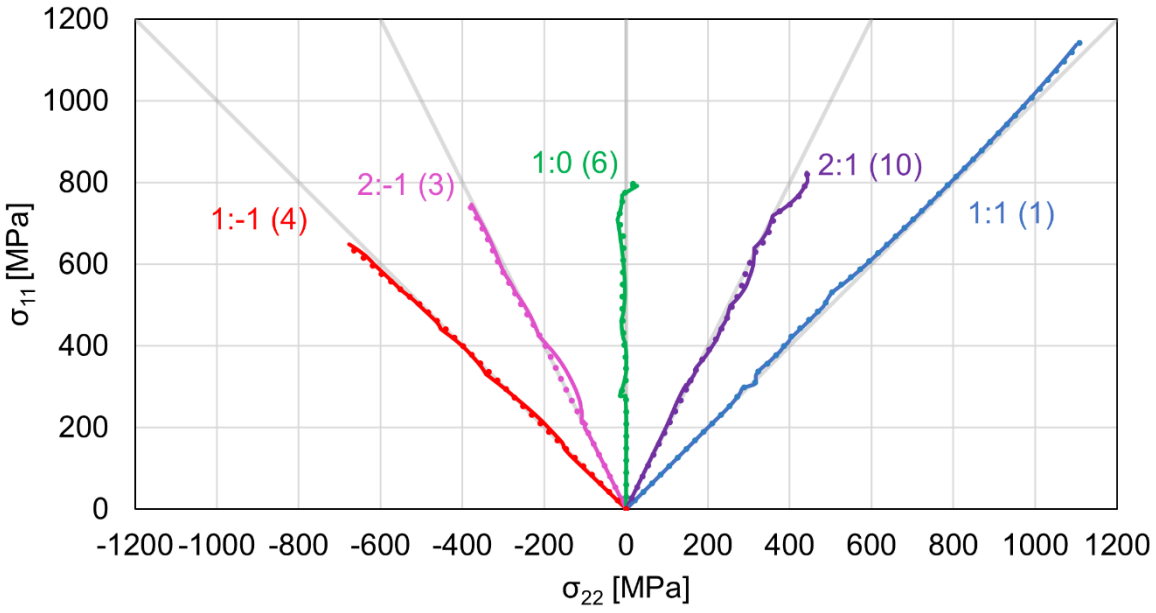

Figure 2.9 Resulting stress produced by interpolated displacement paths. Dotted paths are produced by 750 data point displacement. Solid paths are produced by linearly approximated displacement paths.

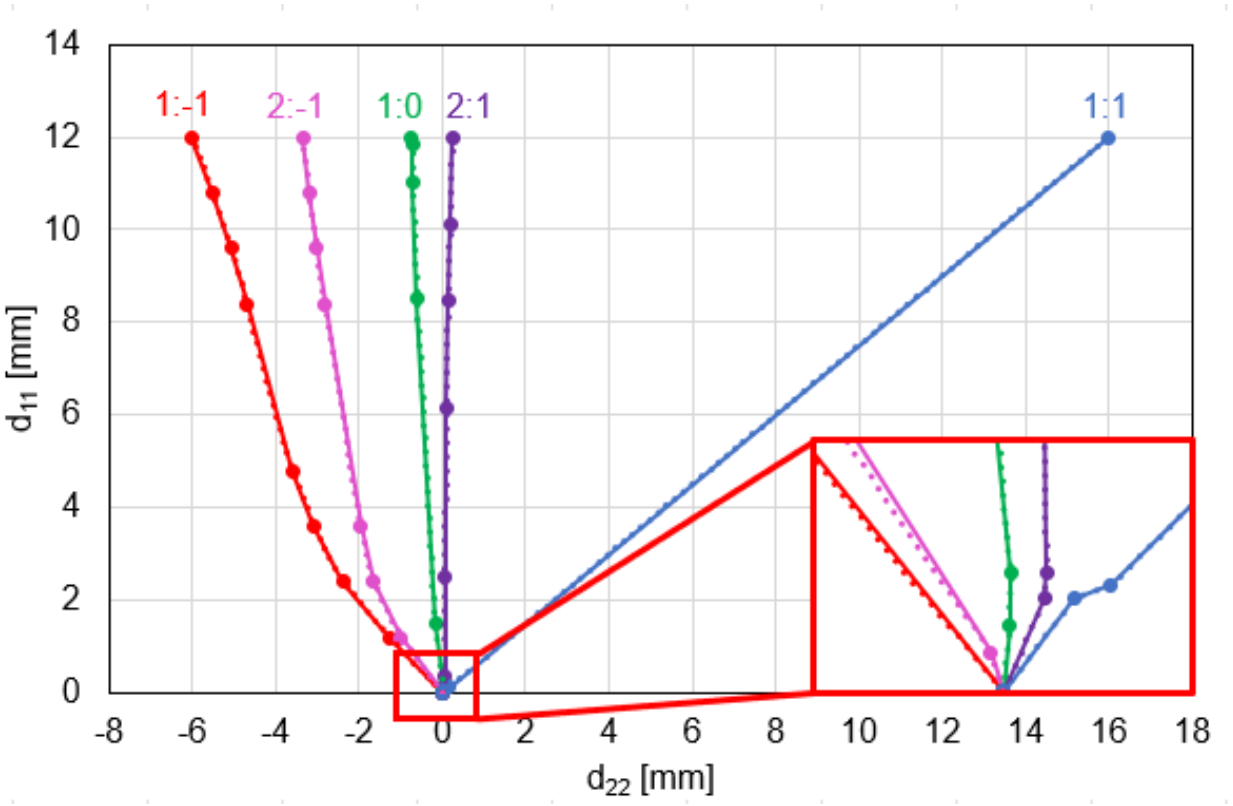

Figure 2.10 Interpolated displacement paths corresponding to five targeted constant stress states. Insert to show elastic region behavior. Dotted paths are 750 data point displacment paths. Solid paths with markers are linearly approximated displacement paths.

The corresponding displacement paths produced by the interpolation calculations were originally comprised of 750 distinct data points. The dotted stress paths in Figure 2.9, the dotted displacement paths in Figure 2.10 and the dotted stress triaxiality in Figure 2.11 are the 750 point displacement path (Figure 2.10) and the corresponding simulation results for stress (Figure 2.9) and stress triaxiality (Figure 2.11). A reduction in displacement path data points was made to simplify future experiments. The University of New Hampshire's biaxial testing frame does not currently accommodate more than nine data entry lines; therefore, the paths were reduced to nine or less increments. The

solid displacement paths shown in Figure 2.10 are comprised of linear segments approximating the interpolated 750 data point displacement paths. The linear approximation is very close to the 750 point curve, with only small deviations. The linearly approximated displacement paths depicted by the solid paths with markers in Figure 2.10 produced the linear stress depicted by the solid curves in Figure 2.9 as well as the stress triaxiality depicted by the solid curves in Figure 2.11. In Figures 2.9, 2.10 and 2.11, the difference between the linear approximation (dotted) and the original 750 data point paths (solid) is small. The use of the reduced data point paths did not alter the results significantly.

Despite minor non-linearities, the simulated stress paths agree well with their respective target path. The agreement is quantified by the difference calculated between the target and simulated stress triaxiality. Figure 2.11 depicts the stress triaxiality with respect to the plastic equivalent strain from each stress state as compared to the target value. Visually, the simulated stress triaxiality (solid lines) appear constant and show only minor differences compared to the target values (dash lines). Errors satisfying termination criteria after interpolation for all five paths are in Table 2.2.

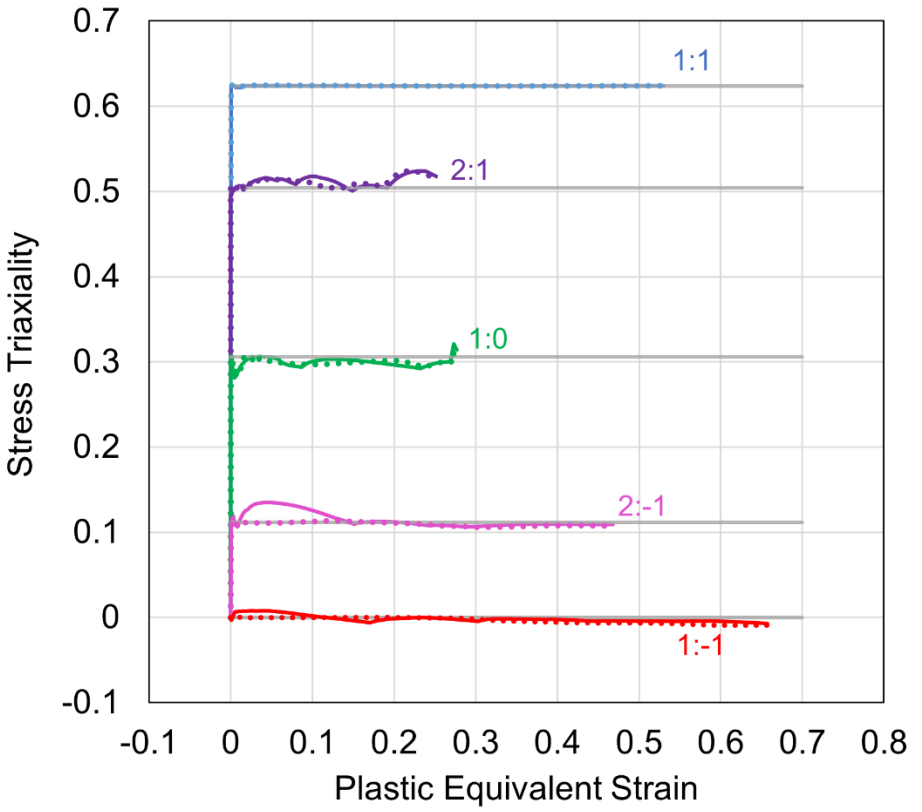

Figure 2.11 Stress Triaxiality extracted from simulations of linearly approximated interpolated displacement (solid lines), and 750 data point displacement path (dotted) compared to target stress triaxiality (gray solid).

Table 2.3 Termination Criteria values for final interpolation of each stress state computed over entire displacement history.

Stress State	Sum Sq. Error	Difference in Sum Sq. Error
1:-1	0.021	0.023
2:-1	0.012	0.010
1:0	0.049	0.011
2:1	0.074	0.029
1:1	1.147E-4	1.444E-5

The elastic to plastic transition that occurs during the cruciform deformation has a significant impact on the displacement curves that produce the linear stress paths. The transition occurs early in the deformation, however the displacement path changes significantly following the transition. The insert in Figure 2.10 depicts a closer view of the displacement paths in the early stage of deformation including the elastic region. There is a concentration of linear segments in this region compared to the remainder of the displacement path.

4. CONCLUSION

An interpolation method to linearize a stress path has been proposed based on non-linear displacement paths. Through several iterations of interpolation, displacement paths are produced in which the resulting stress paths became closer to the target path until acceptable agreement is achieved. Agreement is quantified by an established terminating criterion which measures the difference between the simulated and target stress triaxiality. Five stress states were interpolated successfully in one to ten iterations. Validation of the interpolated paths will be later confirmed through in-plane biaxial cruciform experiments conducted at the University of New Hampshire. From the experiment, force-displacement curves and surface strain fields will be compared with the simulations to validate the results. The development of the interpolated displacement paths eliminates the need for multiple specimen geometries, experimental setups, and data collection systems to study multiple stress states. Further study will be conducted to measure the martensite transformation under various constant stress states.

APPENDICES

A. Progression of termination criteria for stress states

Stress ratio	Iteration	Sum Sq Error	Difference in Sum Sq Error
2:-1	0	4.583	
	1	0.550	4.033
	2	0.022	0.528
	3	0.012	0.010
1:0	0	13.287	
	1	1.799	11.488
	2	0.591	1.208
	3	0.213	0.378
	4	0.194	0.019
	5	0.060	0.134
	6	0.049	0.011
2:1	0	11.0648	
	1	8.346	2.719
	2	3.637	4.709
	3	3.211	0.426
	4	1.471	1.740
	5	0.435	1.036
	6	0.708	0.273
	7	1.149	0.442
	8	0.228	0.921
	9	0.102	0.126
	10	0.074	0.029
1:1	0	1.616E-4	
	1	1.471E-4	1.444E-05

REFERENCES

ABAQUS, 2019. Dassault Systèmes Simulia Corporation, Providence, RI, USA

Adewumi, M., 2020. The Lever Rule. Phase Relations in Reservoir Engineering. John A. Dutton e-Education Institute. Penn State College of Earth Scinece and Minerals Sciences. https://www.e-education.psu.edu/png520/m5_p4.html.

ASTM International, 2016. Standard Test Methods for Tension Testing of Metallic Materials. (ASTM-E8 M) ASTM.

Banerjee, D., Iadicola, M., Creuziger A., Foecke, T., 2015. An Experimental and Numerical Study of Deformation Behavior of Steels in Biaxial Tensile Tests. Miner. Met. Mater. Soc. Eds TMS 2015 144th Annu. Meet. Exhib. https://doi.org/10.1007/978-3-319-48127-2_35.

Barlat, F., Aretz, H., Yoon, J.W., Karabin, M.E., Brem, J.C., Dick, R.E., 2005. Linear transformation-based anisotropic yield functions. Int. J. Plast. 21, 1009–1039. https://doi.org/10.1016/j.ijplas.2004.06.004.

Beese, A.M., Mohr, D., 2011. Effect of Stress Triaxiality and Lode Angle on the Kinetics of Strain-Induced Austenite-to-Martensite Transformation. Acta Materialia 59, 2589-2600.

Besse, A.M., Mohr, D., 2012. Anisotropic Plasticity Model Coupled with Lode Angle Dependent Strain-Induced Transformation Kinetics Law. J. Mech. Phys. Solids 60, 1922-1940.

Creuziger, A., Iadicola, M.A., Foecke, T., Rust, E., Banerjee, D., 2017. Insights into Cruciform Sample Design. JOM 69, 902–906. https://doi.org/10.1007/s11837-017-2261-6.

Deng, N., Kuwabara, T., Korkolis, Y.P., 2015. Cruciform Specimen Design and Verification for Constitutive Identification of Anisotropic Sheets. Exp. Mech. 55: 1005-1022.

Fahr. D., 1971. Stress- and Strain-Induced formation of Martensite and its Effects on Strength and Ductility of Metastable Austenitic Stainless Steels. Metallurgical Transactions 2: 188-1892.

Geijselaers, H.J.M., Hilkhuijsen, P., Bor, T.C., Perdahcioglu, E.S., van den Boogaard, A.H., 2013. Modelling of the Austenite-Martensite Transformation in Stainless and TRIP Steels. AIP Conference Proceedings 1532, 175. https://doi.org/10.1063/1.4806822.

Gerke, S., Adulyasak, P., Brünig, M., 2017. New biaxially loaded specimens for the analysis of damage and fracture in sheet metals. Int. J. Solids Struct. 110–111, 209–218. https://doi.org/10.1016/j.ijsolstr.2017.01.027

Giannella, V., Dhondt, G., Kontermann, C., Citarella, R., 2019. Combined static-cyclic multi-axial crack propagation in cruciform specimens. Int. J. Fatigue 123, 296–307. https://doi.org/10.1016/j.ijfatigue.2019.02.029

Hanabusa, Y., Takizawa, H., Kuwabara, T., 2010. Evaluation of Accuracy of Stress Measurements Determined in Biaxial Stress Tests with Cruciform Specimen Using Numerical Method. Steel Research International (81) 9, 1376-1379.

Hanabusa, Y., Takizawa, H., Kuwabara, T., 2013. Numerical verification of a biaxial tensile test method using a cruciform specimen. J. Mater. Process. Technol. 213, 961–970. https://doi.org/10.1016/j.jmatprotec.2012.12.007

Hannon, A., Tiernan, P., 2008. A Review of Planar Biaxial Tensile Test Systems for Sheet Metal. J. Mat. Proc. Tech. 198, 1-13.

Hockett, J.E., Sherby, O.D., 1975. Large strain deformation of polycrystalline metals at low homologous temperatures. J. Mech. Phys. Solids 23, 87–98. https://doi.org/10.1016/0022-5096(75)90018-6

Hoffman, J., Banerjee, D., Iadicola, M., "Determination of Strain Path Envelope in an Optimized Biaxial Cruciform Specimen of AISI 1008 Steel under Linear, Bilinear, and Nonlinear Strain Paths"*, The Materials Society Conference* 2022

Hou, Y., Min, J., Lin, J., Carsley, J.E., Stoughton, T.B., 2018. Cruciform specimen design for large plastic strain during biaxial tensile testing. J. Phys. Conf. Ser. 1063, 012160. https://doi.org/10.1088/1742-6596/1063/1/012160

International Organization for Standardization, 2014. Metallic materials — Sheet and strip — Biaxial tensile testing method using a cruciform test piece (ISO 16842). ISO.

Kuwabara, T., Ikeda, S., Kuroda, K., 1998. Measurement and analysis of differential work hardening in cold-rolled steel sheet under biaxial tension. J. Mater. Process. Technol. 80–81, 517–523. https://doi.org/10.1016/S0924-0136(98)00155-1

Liu, J., 2016. Deformation Induced Martensitic Transformation In 304 Stainless Steels. (Master's Thesis). Retrieved from https://scholarcommons.sc.edu/etd/3804.

Mamros, E.M., Mayer, S.M., Banerjee, D.K., Iadicola, M.A, Kinsey, B.L., Ha, J., 2022. Evolution of Plastic Anisotropy of SS316L Under Proportional Loading and Modeling for In-Plane Biaxial Tension.

Nasdala, L., Husni, A. H., 2020. Determinatio of Yield Surfaces in Accordance with ISO 16842 Using an Optimized Cruciform Specimen. Exp. Mech. 60(2). DOI: 10.1007/s11340-020-00601-9.

Nikhare, C.P., Vorisek, E., Nolan, J.R., Roth, J.T., 2017. Forming Limit Differences in Hemispherical Dome and Biaxial Test during Equibiaxial Tension on Cruciform. J. Eng. Mater. Tech., 139(4): 041011.

Olson, G.B., Cohen, M., 1975. Kinetics of Strain-Induced Martensitic Nucleation. Metall. Trans. A. 6, 791.

Stringfellow, R.G., Olson, G.B., Parks, D.M., 1992. A Constitutive Model for Transformation Plasticity Accompanying Strain-Induced Martensitic Transformations in Metastable Austenitic Steels. Acta Metall. Mater. 40, 1703-1716.

Talonen, J., Aspegren, P., Hanninen, H., 2004. Comparison of Different Methods for Measuring Strain Induced α'- Martensite Content in Austenitic Steels. Materials Science and Technology 20, 1506-1512.

Wang, H., Xu, T., Shou, B., 2016. Determination of Material Strengths by Hydraulic Bulge Test. Materials 2017, 10(1), 23.

Yanaga, D, Kuwabara, T., Uema, N., Asano, M, 2012. Material Modeling of 6000 Series Aluminum Alloy Sheets with Different Density Cube Textures and Effect on the Accuracy of Finite Element Simulation. Int. J. Solids and Structures, 49 25, 3488-3495.

Yin, Q., Kolbe, J., Haupt, M., Tekkaya, A.E., 2013. Achieving High Strains in Sheet Metal Characterization Using the In-Plane Torsion Test. Key Eng. Mat. 554-557. pp. 77-85.

Zhao, K., Chen, L., Xiao, R., Ding, Z., Zhou, L., 2019. Design of a biaxial tensile testing device and cruciform specimens for large plastic deformation in the central zone. J. Mater. Sci. 54, 7231–7245. https://doi.org/10.1007/s10853-019-03358-2